Check for updates

On the formation of porosity in hydroxyapatite/polyester high-velocity oxygen-fuel sprayed coatings and their electrochemical behavior in simulated body fluid

Juan Carlos Jamboos Toledo[1] · John Henao[2] · Carlos A. Poblano-Salas[1] · Astrid L. Giraldo-Betancur[3] · Diego German Espinosa-Arbelaez[4] · Jorge Corona Castuera[1] · Oscar Sotelo Mazón[5]

Abstract

Orthopedic implants play a crucial role in restoring the function and life quality of the population with musculoskeletal disorders. However, implant failure and lack of integration with the surrounding bone tissue, mainly in patients with low bone quality, remain significant challenges in biomedicine. Porous bioactive coatings have emerged as a promising approach to address these issues. This work aims to explore the feasibility of preparing porous hydroxyapatite coatings by high-velocity oxy-fuel spray (HVOF) and, as a first approach, to evaluate the performance of the porous bioactive coatings obtained in simulated body fluid for a possible application in orthopedic surfaces. This paper discusses the use of polyester as a pore-forming agent and the importance of some relevant factors, such as coating fabrication parameters and post-spraying treatments, for producing porosity in the coatings. The results display the formation of different degrees of porosity ranging from 3.8% to 38% depending on the weight fraction of the pore-forming phase employed to prepare the hydroxyapatite coatings. The coatings were evaluated in Hanks balanced solution at body temperature by employing different electrochemical techniques; interestingly, the results suggest different bioactive responses as a function of porosity.

1 Introduction

Orthopedic implants, such as joint replacements and bone fixation devices, have revolutionized the field of orthopedics for decades. Their long-term success relies on achieving strong implant–bone integration [1, 2]. Many multinational companies offer today reliable orthopedic implants, having up to 95% implant survival in long-term clinical follow-up studies [3]. Several factors influence the long-term survival of orthopedic implants, among them patient-related factors play a significant role [4]. Some patient-related factors associated with higher long-term orthopedic implant survival are age, good general health, body mass index (BMI), or non-smoking status. For instance, young patients generally have better implant survival rates than older individuals. This fact is attributed to better bone quality, higher activity levels, and fewer comorbidities. Younger patients often experience less wear and tear on the implant and have a higher capacity for bone regeneration and remodeling [5]. Patients with good overall health, i.e., well nourished, free of systemic diseases, and with well-managed chronic conditions, tend to have better implant survival. Systemic diseases such as diabetes, rheumatoid arthritis, and autoimmune disorders can impact bone health and impair healing [6, 7], increasing the risk of complications and implant failure. Patients with normal weight and BMI tend to have better outcomes

✉ Carlos A. Poblano-Salas
carlos.poblano@ciateq.mx

1   CIATEQ A.C., Av. Manantiales 23-A, Parque Industrial Bernardo Quintana, El Marqués, 76246 Querétaro, México

2   CONAHCYT-CIATEQ A.C., Av. Manantiales 23-A, Parque Industrial Bernardo Quintana, El Marqués, 76246 Querétaro, México

3   CONAHCYT-Cinvestav, Libramiento Norponiente # 2000, Fraccionamiento Real de Juriquilla, 76230 Querétaro, México

4   CIDESI, Centro de Investigación y Desarrollo, Av. Pie de la Cuesta 702, 76125 Querétaro, México

5   Universidad Autónoma de Morelos (UAEM), Av. Universidad No. 1001, Chamilpa, 62209 Cuernavaca, MOR, México

than those who are overweight. Excessive body weight can exert additional stress on the implant, leading to increased wear and loosening [8]. It can also negatively affect the bone quality and healing process. Similarly, smoking has been associated with an increased risk of complications; for instance, it reduces blood flow, impairs tissue healing, and negatively affects bone metabolism. Non-smoking patients have better implant survival rates and fewer post-operative complications [9].

Although success of orthopedic implants depends on several factors, survival rate statistics of many commercial devices are mostly negatively influenced due to the complications presented in patients with deficient bone health. In this sense, several efforts have been made to improve the performance of orthopedic implants from many different points of view, including metallurgy of the alloys, the introduction of additively manufactured cellular structures, the use of bone cements, the development of bioactive coatings, among others [10]. Since the 80s, hydroxyapatite (HAp) coatings were introduced to improve metallic implant osseointegration in the human body due to the ability of HAp to promote bone regeneration. Since then, HAp coatings have been known within the biomedical industry and various successful clinical follow-up studies have been published [11–14]. In particular, plasma-sprayed HAp coatings are currently the most accepted option within the biomedical industry due to the good clinical results reported in the last 3 decades [15, 16]. However, in recent years, the high-velocity oxygen-fuel spray (HVOF) technique has emerged as an excellent alternative to replace plasma-sprayed HAp coatings, since HVOF can promote the formation of more chemically stable phases in the coating with respect to those produced by plasma spray, resulting in a modulated interaction of the implant in physiological fluids [17]. Plasma spray and HVOF are both thermal spray processes used for surface coating and material deposition. They are widely employed in various industries, including aerospace, automotive, energy, and biomedical. Plasma spraying involves the creation of a high-temperature plasma jet by ionizing a gas with an electric arc, where the coating material is injected into the plasma jet, heated, and propelled into the substrate surface to generate the coating. This technique is usually employed for ceramic materials, as the plasma temperature achieves a temperature well above 5000 °C.

On the other hand, HVOF is a thermal spray technique that employs a combustion process, achieving temperatures up to 3200 °C. Here, the combustion gases are accelerated through a converging–diverging nozzle and the powder is propelled onto the substrate surface at high velocities. Then, the particles impact the substrate at high speeds, deform, and adhere to form a dense and well-bonded coating. The flame temperatures achieved in the HVOF process are far lower than those attained in plasma spraying; therefore, the

formation of metastable phases from the HAp in the coatings is avoided. Such phases are formed due to the high solidification rates present when the in-flight particles hit the substrate. In plasma-sprayed coatings, the solidification rates are larger resulting in the formation of metastable phases such as amorphous calcium phosphate, calcium oxide, tetra calcium phosphate, and tricalcium phosphate, which show larger dissolution rates in body fluids than HAp [18]. Another advantage of the HVOF process over plasma spraying is the use of less sophisticated equipment which makes it more affordable and easier to operate. Other advantages of HVOF sprayed coatings are their high density and low porosity, resulting in improved mechanical properties, which can benefit the long-term survivability of coated surfaces in the biomedical field [19]. Several reports have been published in recent years about the in-vitro behavior of HVOF-sprayed HAp coatings [17, 19–22]. However, no clinical outcomes arising from the use of such coatings have been reported so far.

Bearing in mind the different factors affecting implant rate survivability, bone health is crucial for remodeling and fixation of the tissue surrounding the surface of an implant. In low-bone-quality patients, the decreased bone mass reduces the available surface area for implant–bone contact, limiting the potential for strong fixation. Poor bone health affects the quality of bone tissue, including changes in mineralization, collagen structure, and bone turnover. Altered mineralization reduces the bone´s strength and stiffness, while collagen structure changes affect its elasticity and resilience. In addition, disrupted bone remodeling processes result in an imbalance between bone resorption and formation, leading to compromised bone healing and integration with the implant [23, 24].

Considering these biological factors, strategies to enhance implant fixation in patients with low bone health may involve promoting bone formation and remodeling, improving vascularity, and optimizing the bone–implant interface. This fact can be achieved using bone grafts or bone substitutes, surface modifications of the implant to enhance osteointegration, and applying growth factors or bone-stimulating agents to stimulate bone healing and regeneration [25]. Particularly, porous bioactive coatings offer a unique solution for low-bone-quality patients by providing an interconnected pore network that promotes osseointegration and enhances the biological response of the implant [26]. Porous bioactive coating promotes osseointegration by placing a bioactive material on the top surface of the implant, boosting the natural remodeling process. The porosity of implants may enhance the integration and long-term stability of the implant within the compromised bone tissue. Porous coatings on the top surface of implants provide a larger surface area than solid uncoated implants. The increased surface area provides more contact points for bone–implant interaction [24]. In low bone quality conditions, where the available bone surface for implant fixation may be limited, the

greater surface area of porous implants improves the potential for bone apposition/ and integration and can enhance stability. The porous structure of implants allows for mechanical interlocking between the implant and bone tissue. Bone grows into the pores and interlock with the implant, creating a strong bond. This mechanical interlocking helps to resist implant loosening and provides additional stability in low-bone-quality situations. Due to bone in-growth, porous coatings help to distribute loads more evenly across the implant–bone interface and facilitate the exchange of nutrients, oxygen, and cells involved in the healing process. It is important to note that the porosity of coated implants should be carefully designed to balance structural integrity and mechanical strength with optimal porosity levels for bone integration. Based on early studies regarding porous bioactive scaffolds, the minimum pore size requirement is about ~100 μm due to cell size, migration, and transport. Pore sizes larger than 300 μm are also recommended to improve bone formation [27]. However, recent studies [28, 29] about biomimetic coating techniques suggest that pore size below ~100 μm can also support osteoblast cell adhesion and proliferation and facilitate good bonding between the coating and substrate.

The present work is an effort to explore the feasibility of creating artificial porosity within thermal-sprayed bioactive coatings by employing a porous-forming phase. Porosity in thermal spray coatings, particularly HVOF, is often below 10% in volume, with pore sizes below 10 μm due to the high impact velocities achieved by the particles during deposition. Previous studies [30] employing vacuum plasma spray have proposed the use of encapsulated water on the surface of the substrate which, during the deposition of the coating, undergo evaporation creating a sort of channels that can be used to the transport of species from the surroundings into the coating. However, this solution requires excellent control of sites where water is absorbed on the implant's surface to avoid risks to the mechanical integrity of the coated surface in service. This solution also exposes the metal surface directly to the body fluids, increasing the risk of ion dissolution that may affect cell adhesion and proliferation. The strategy proposed in the present work seeks a hybrid solution between a conventional HVOF thermally sprayed bioactive coating and a porous scaffold, remarking that this approach is a first step for future studies that may consider the present results to find out the limits of porous-forming ability and performance of this kind of coatings.

2 Experimental section

2.1 Feedstock powder and substrates

This study employed a commercial hydroxyapatite (HAp) powder (Captal 30SD, Plasma Biotal, UK) to prepare HAp-based coatings. Commercial polyester (PS) powder (Metco 600NS-1) was employed as the pore-forming phase. In addition, the coatings included a bondcoat layer of TiO_2. To include the pore-forming phase into the HAp coatings, HAp-PS powder mixtures were prepared in a roll-mixer at a rotational speed of 350 rpm. Three powder mixtures were proposed namely HAp-10 wt% PS, HAp-20 wt.% PS, and HAp-30 wt.% PS. The powders were blended during 2 h, 4 h, and 8 h to evaluate the optimal blending time. To determine the level of fluidity of the powder mixtures, the Hausner ratio (HR) was calculated from the bulk density and the apparent tapped density of the powders, following the rule of mixtures for mass density [31]. Scanning electron microscopy (SEM, Jeol IT100) and energy-dispersive X-ray spectroscopy (EDS) analysis were performed on the powder blends to study their morphology and elemental composition, respectively. The structural characterization of the powders was carried out by X-ray diffraction (XRD) using a diffractometer (Rigaku, Smart Lab) with Cu K α radiation (l = 0.154060 nm), a scanning speed of 4° per min, and a step size of 0.02°. The particle size distribution of the powders was obtained by laser diffraction (HELOS/BR, Sympatec GmbH) following a dry dispersion method. Thermogravimetric analysis (TGA) (TA Instruments Q600) was carried out in the PS powder at a scanning rate of 10 °C/min between room temperature and 600 °C in order to reveal its thermal decomposition process and degradation temperature. Ti-6Al-4 V substrates ($2 \times 2 \times 2$ cm) were employed to spray the HAp-PS coatings. The substrates were previously ground with 240 grit sandpaper and grit-blasted with 20 grit Al_2O_3 to remove oxide layers and achieve the required roughness (Ra = 5 μm) to promote mechanical anchoring during thermal spraying. Before spraying, the substrates were ultrasonically cleaned with ethanol to remove impurities from the grit blasting process.

2.2 Thermal spray coating preparation

This study employed the High-Velocity Oxygen-Fuel (HVOF) spray process (DJ2700 hybrid gun, Oerlikon Metco) to obtain the HAp and HAp-PS coatings [32]. The HVOF gun was mounted in a 6-axis robotic arm (Kuka, GmBH) that allows control of some variables of the process, such as the stand-off distance (SOD), the relative velocity (raster speed) between the nozzle exit of the HVOF gun and the substrate surface, and the number of spraying passes. The powders were sprayed by employing a powder feeder (Thermach Inc, USA) with a feeding rate of 15 g/min. The type of powder mixture was set as an input variable, while the SOD, raster speed, fuel/oxygen ratio, and substrate preheating were set as constant values of 200 mm, 1 m/s, 0.14, and 300 °C, respectively, as reported elsewhere [20]. A summary of parameter combinations is presented in Table 1. The

following spraying conditions were employed for producing the TiO$_2$ bond coat: 250 mm SOD, 0.21 fuel/oxygen ratio, 1 m/s raster speed, and 10 g/min feed rate, as previously reported in the literature [19]. A schematic diagram of the process followed for the preparation of coatings is presented in Fig. 1.

2.3 Coatings characterization

Samples were sectioned perpendicular to the coating surface using a diamond cutting disc for metallographic preparation. The samples were prepared according to the ASTM E1920 standard. All specimens were cold mounted with an epoxy resin, ground, and polished with alumina powder to obtain a mirror-polished surface. Optical microscopy (MO, Keyence VHX 6000) and SEM analysis were carried out for microstructural observation and porosity determination. The porosity level was determined according to the ASTM E2109 standard from cross-sectional images of the coatings and using the Image J software. The reported porosity value

is the average porosity percentage obtained from 5 images. Surface roughness of coatings and substrate was measured using a surface roughness gage stylus (Mitutoyo, SURFT-EST SJ-310). Roughness values of the samples are presented as an average value of 5 measurements on each surface. The interfacial adhesion of the coatings was measured by following a procedure described elsewhere [19]. In particular, this property was measured on HAp coatings without exposure to simulated body fluid and at the HAp-TiO$_2$ interface.

2.4 Post-spraying treatments

The as-sprayed coatings were heat treated at 600 °C to remove the pore-forming phase (PS phase) for 1 h, 4 h, and 8 h and cooled in a furnace (KSL-1700 A3) until room temperature was achieved. Subsequently, the samples were immersed in xylene to remove traces of the PS for 1 h. Finally, the coatings were washed with ethanol and air-dried at room temperature. The porosity of the coatings was also measured by following the ASTM E2109 standard after removing the pore-forming phase to get a direct comparison of the porosity evolution due to the post-spraying treatment.

2.5 Electrochemical evaluation in simulated body fluid

Electrochemical analysis of the substrate and the coatings was performed under in-vitro conditions in simulated body fluid (SBF, Hank's balanced salt solution) at body

Table 1 Combination of conditions for coatings deposition

Coating's ID	SOD (mm)	Sprayed powders
H0	200	HAp
H1		HAp-10wt.%PS
H2		HAp-20wt.%PS
H3		HAp-30wt%.PS
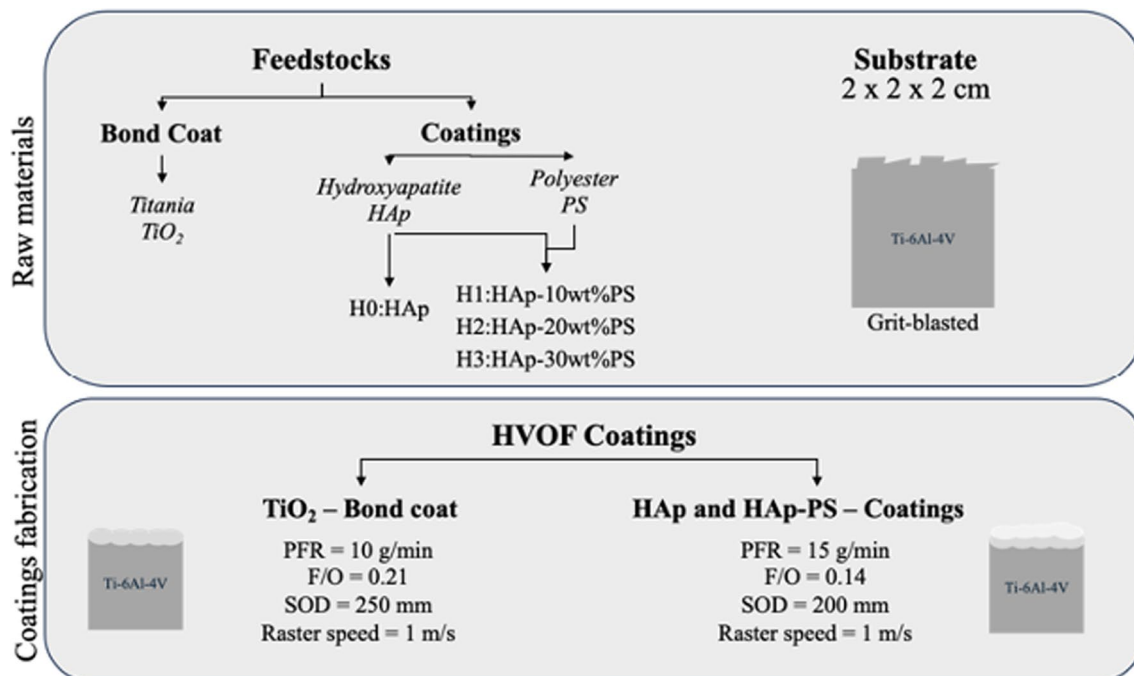
Fig. 1 Diagram of the process followed for the preparation of HAp-PS coatings

temperature (~ 36.5 °C). Measurements were performed in a Potentiostat/Galvanostat (Gamry, Interface 1000E) with a flat three-electrode cell following the ASTM F2129 standard. The substrate and the coating sample were employed as the working electrode, a saturated calomel electrode (SCE) as the reference electrode, and a graphite rod as the auxiliary electrode. In all cases, the sample area exposed to the electrolyte solution was 1 cm^2. Open circuit potential and electrochemical impedance spectroscopy (EIS) measurements were performed. Prior to the electrochemical tests, all the samples were UV sterilized for 12 h. The measurements were continuously performed for 28 days to study the interaction between the coated surface and the SBF. At the end of the soaking cycle, Ti-6Al-4 V and HAp/TiO$_2$ graded coatings were rinsed with distilled water and dried at room temperature. EIS measurements were performed at open circuit potential with the amplitude of the sinusoidal signal set at ± 10 mV rms. EIS spectra were acquired in the 0.01–30,000 Hz frequency range, recording six points per frequency decade. Impedance spectra were represented in both complex impedance (Nyquist plot) and Bode (amplitude and phase angle plots) diagrams to evaluate the electrochemical behavior of the samples.

3 Results and discussion

Figure 2 presents the morphology and particle size distribution for each of the powders used in this study. Figure 2a shows that the HAp powder has an irregular morphology,

typical of agglomerated powder composed of submicron-sized particles that have been sintered. The HAp powder exhibits a monomodal particle size distribution (Fig. 2d) and has d$_{10}$, d$_{50}$, and d$_{90}$ values of 11 µm, 24 µm, and 38 µm, respectively. This type of HAp powder has also been reported in previous studies for the fabrication of HVOF-sprayed coatings [19, 20]. This kind of powder exhibit good flowability, enabling the fabrication of HAp-sprayed coatings with densities exceeding 95%.

Figure 2b shows the morphology of the TiO$_2$ powder employed in the fabrication of the bond coat layer. The TiO$_2$ bond coat is typically sprayed to reduce the residual stress level that is induced due to the difference in thermal expansion coefficients between HAp and the Ti-6Al-4 V substrate, and to improve adhesion of HA-based coatings on Ti surfaces [33]. The TiO$_2$ powder exhibits a dense irregular morphology typical of crushed and sintered powders. This powder also presents a monomodal particle size distribution (Fig. 2e) with d$_{10}$, d$_{50}$, and d$_{90}$ values of 6.7 µm, 17 µm, and 26 µm, respectively. According to previous studies [20], an irregular morphology and a particle size distribution between 6 µm and 26 µm are ideal for fabricating TiO$_2$ coatings sprayed on Ti-6Al-4V substrates by HVOF thermal spray. This particle size distribution allows for the formation of dense coatings by ensuring the complete melting of the particles in the HVOF process, forming layers of molten material that, through successive splats stacking, promote the formation of a compact coating structure [34].

Figure 2c shows the morphology of the PS powder used as a pore-forming material for the fabrication of HAp
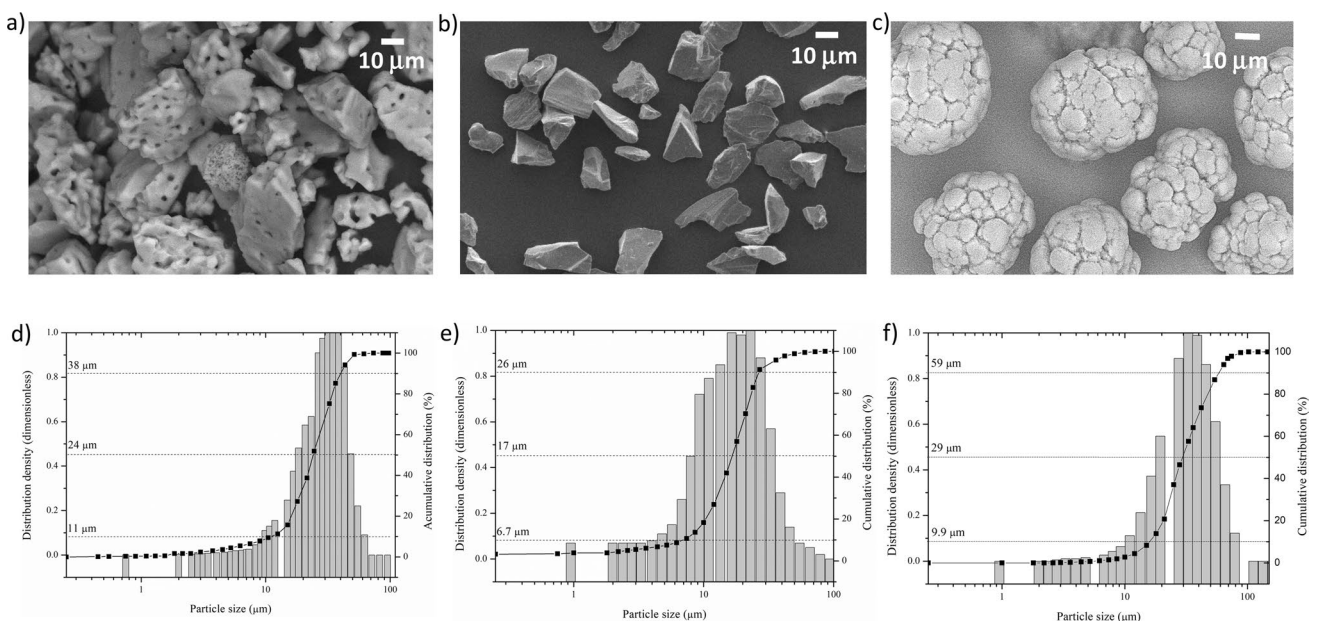

Fig. 2 **a** SEM images of the HAp powder, **b** Titania powder, **c** PS powder, **d** particle size distribution (PSD) of the HAp powder, **e** PSD of the PS powder

coatings by the HVOF process in this study. The PS powder has a spherical morphology and a monomodal particle size distribution with d_{10}, d_{50}, and d_{90} values of 9.9 μm, 29 μm, and 59 μm, respectively (Fig. 2f). Specifically, the PS powder (600-NS1, Oerlikon Metco) is commercially offered to produce self-lubricating coatings by atmospheric plasma spray (APS). This powder is also recommended for the fabrication of abradable coatings, where the PS acts as a fugitive phase, being burned out in the presence of a ceramic phase to achieve a porous ceramic abradable coating structure. The same principle was applied in the present work for obtaining porous HAp coatings by HVOF thermal spray, as further described below.

Figure 3 presents the diffraction patterns of HAp, TiO_2, and PS powders used in this study. The HAp powder in Fig. 3a exhibits a diffraction pattern characteristic of crystalline HAp, as evidenced by comparing the experimental diffraction spectrum with the standardized HAp pattern

(PDF 090432), with the absence of secondary phases. The lattice parameters of the HAp unit cell and the Ca/P ratio were estimated through Rietveld refinement, yielding values of 9.425 Å and 6.875 Å for the $a = b$ and c parameters, respectively, and a Ca/P ratio of 1.66. According to previous reports [35], it is known that the suggested Ca/P ratio of HAp for surgical implants falls within the range of 1.65 to 1.82, with a Ca/P ratio of 1.65 being the closest to that of human bone [36].

The XRD pattern of TiO_2 powder is presented in Fig. 3b. The comparison of the experimental TiO_2 spectrum with the standardized pattern reveals the presence of rutile (PDF-211276), anatase (PDF-211272), and Magnelli phases (PDF-500787). The rutile phase has a tetragonal structure, with a unit cell containing two units of TiO_2, where each oxygen atom is coordinated with three titanium atoms. The presence of the rutile phase in molten TiO_2 powders is commonly reported (solidification temperature 1840 °C), as it
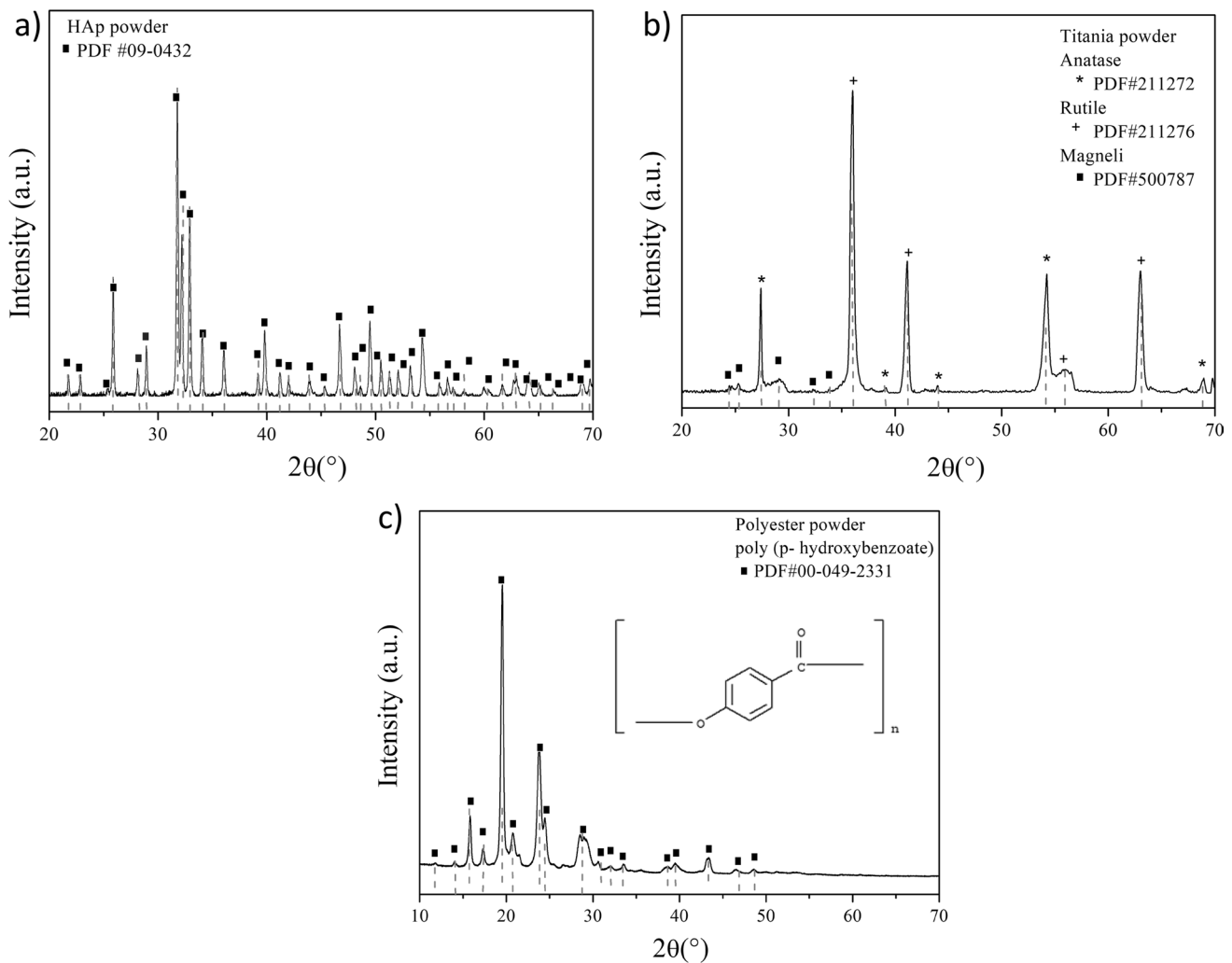

Fig. 3 **a** XRD pattern of the HAp powder, **b** XRD pattern of the titania powder, **c** XRD pattern of the PS powder

is the most stable form of TiO_2 [37]. On the other hand, the anatase phase also exhibits a tetragonal structure, but its unit cell contains four units of TiO_2, and each oxygen atom is coordinated with three titanium atoms. The presence of anatase phase can also occur during solidification of molten TiO_2 powders since it is a metastable phase which can be formed due to factors such as cooling conditions and working pressures [37, 38]. Both anatase and rutile phases are well-known for their bioactive properties in physiological environment, promoting the formation of HAp [39]. This bioactive behavior is based on the interaction of rutile and anatase with reactive oxygen and nitrogen species released by macrophages in the human body [40]. Finally, the Magnelli phases are non-stoichiometric structures ($TinO_2n$-1; $n = 4$–10) derived from rutile and are characterized by the presence of oxygen and titanium vacancies. The presence of Magnelli phases in molten TiO_2 powders is often attributed to oxygen-deficient atmospheres during the solidification process. Magnelli phases can also be biocompatible; for instance, phases like Ti_4O_7 and Ti_5O_9 are commercially known as EBONEX and are employed in biomedical applications due to their good biocompatibility [40, 41].

The XRD pattern of the PS powder is shown in Fig. 3c. The results indicate that this powder is a crystalline polymer with the structure of the poly(p-hydroxybenzoate), PDF-00-049-2331. Polyesters are a family of polymers that contain an ester functional group (O=OR) within each repeating unit of the polymer chain. One of the most well-known polyesters in the market is polyethylene terephthalate (PET), which is used in the manufacturing of beverage containers for human consumption [42]. The poly(p-hydroxybenzoate) is a polyarylate, which is a type of aromatic polyester. Due to its molecular structure, the poly(p-hydroxybenzoate) is known for its high chemical stability, bioinertness, and high melting point (405 °C). These properties make this polymer suitable for applications in the automotive and biomedical sectors [43].

Figure 4 shows SEM/EDS images of HAp and PS powders blends prepared for mixing time periods between 2 and 8 h. Figure 3a, b, and c shows the images of the HAp 10 wt.% PS powder after 2 h, 4 h, and 8 h of mixing, respectively. The red areas visible in Fig. 4c correspond to carbon elemental analysis in the samples, which can be attributed to the presence of the PS organic phase in the mixtures. Notably, as the mixing time increases from 4 to 8 h, HAp-PS particle agglomerates appear. Interestingly, as shown in Fig. 4c, the PS particles act as a ductile phase onto which the HAp particles adhere. This behavior is also observed for the HAp 20 wt.% PS and HAp 30 wt.% PS mixtures, as shown in Fig. 4d, e, respectively. Previous studies [44] have suggested that long mixing times (> 4 h) promote deformation of polymeric particles, leading to the formation of agglomerated particles in attrition-milled mixtures. The formation of large agglomerates (as observed after 8 h mixing in this work) may impact powder flowability, leading to the formation of non-homogeneous coatings. In the present study, the Hausner ratio (HR) was determined for each powder, yielding values of 1.14, 1.16, 1.27, 1.28, and 1.26 for the HAP 10 wt.% PS mixtures prepared at 2 h, 4 h, 8 h, and HAp 20 wt.% PS and HAp 30 wt.% PS mixtures prepared at 8 h, respectively. A HR greater than 1.19 generally indicates poor flowability [31], which can result in either intermittent powder flow during HVOF spraying or clogging of the feeding conduits of the feedstock powder injection system. Hence,
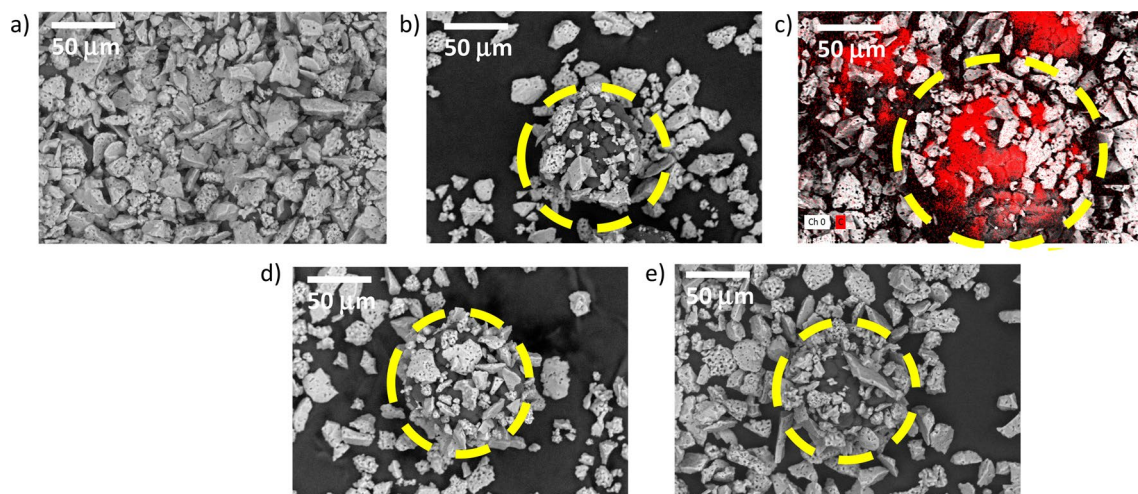
Fig. 4 SEM images of HAp-10wt.%PS powder mixture after **a** 2h mixing, **b** 4h mixing, **c** 8h mixing. Red points in **c** refers to the carbon content associated with the presence of polyester forming large agglomerates. **d** HAp-20wt.%PS powder mixture after 4h mixing, **e** HAp-30wt.%PS powder mixture after 4h milling. Yellow dashed lines display the formation of HAp/PS agglomerates. Colored red areas in **c** display the presence of carbon associated with the PS phase

the HAp-PS powder mixtures prepared at 8 h were deemed unsuitable for use as feedstock material in the present study.

Figure 5 shows the particle size distribution for the HAp-PS powder blends prepared at 2 h and 4 h. It can be observed that the mixtures prepared at 2 h exhibit a monomodal distribution (Fig. 5a, b, and c), with a slight increase in d_{50} and d_{90} values as the percentage of PS added to HAp increases. The d_{50} value increased from 25 μm in the HAp 10 wt.% PS mixture to 27 μm in the HAp 30 wt.% PS mixture, whereas the d_{90} value increased from 39 μm in the HAp 10 wt.% PS mixture to 49 μm in the HAp 30 wt.% PS sample. The increase in d_{50} and d_{90} values in the mixtures prepared at 2 h can be attributed to the contribution of the larger particle size of PS added to HAp and the absence of agglomerate formation, Fig. 4a. On the other hand, when the mixtures were prepared at 4 h (Fig. 5d, e, f), a bimodal particle size distribution was obtained. This result complements the observations in Fig. 4, where agglomerates are observed after 4 h of mixing. These agglomerates form larger particles in which HAp surrounds the PS particles. Consequently, an increase in d_{50} and d_{90} values is registered in the powders mixed at 4 h when compared to those mixtures prepared at 2 h, with values ranging from 24 to 51 μm and 31 to 59 μm, respectively, The HR exhibited values of 1.16, 1.15, and 1.17 for the HAp 10 wt.% PS, HAp 20 wt.% PS, and HAp 30 wt.% PS mixtures prepared at 4 h, respectively, suggesting good flowability for these powders. It is important to mention that due to the characteristics of the HVOF thermal spray process [45], where particles are injected into a supersonic flame, it

is crucial for the powder mixtures to be cohesive (mechanical adherence) or adhesive (electrostatic adherence) [46], especially when the materials involved have different densities. This condition is crucial to avoid differences in trajectories, velocities, and residence times in the flame, which can result in coating features such as porosity, cracks, or lack of thickness uniformity [47]. Thus, monomodal powders obtained in this study were employed for the fabrication of the HAp-PS coatings.

Figure 6 shows the cross-sectional view of the HAp (H0) and HAp-PS coatings (H1, H2, and H3) obtained by HVOF. In Fig. 6a, a cross-sectional view of the H0 coating is presented. This coating exhibits a bi-layer architecture, with a top layer of HAp and a TiO_2 bond coat on the Ti-6Al-4 V substrate. The HAp coating displays typical microstructural characteristics of HVOF-sprayed coatings, with the presence of molten and semi-molten particles, as well as the presence of pores. Figure 6b, c, and d shows the H1, H2, and H3 coatings, respectively. Two types of deposited particles are identified in the coatings. The dark-colored particles (arrows in Fig. 6b, c and d) correspond to the PS phase, while the gray particles surrounding the dark-colored ones correspond to the HAp phase. An increase in the presence of rounded HAp particles is observed in H1, H2, and H3 coatings compared to the H0 coating. In fact, coating build up consists of stacking both PS and HAp particles with a high kinetic energy. The morphology of the PS was not maintained due to the high velocity impact, but it worked as a ductile phase as some HAp particles were embedded in the
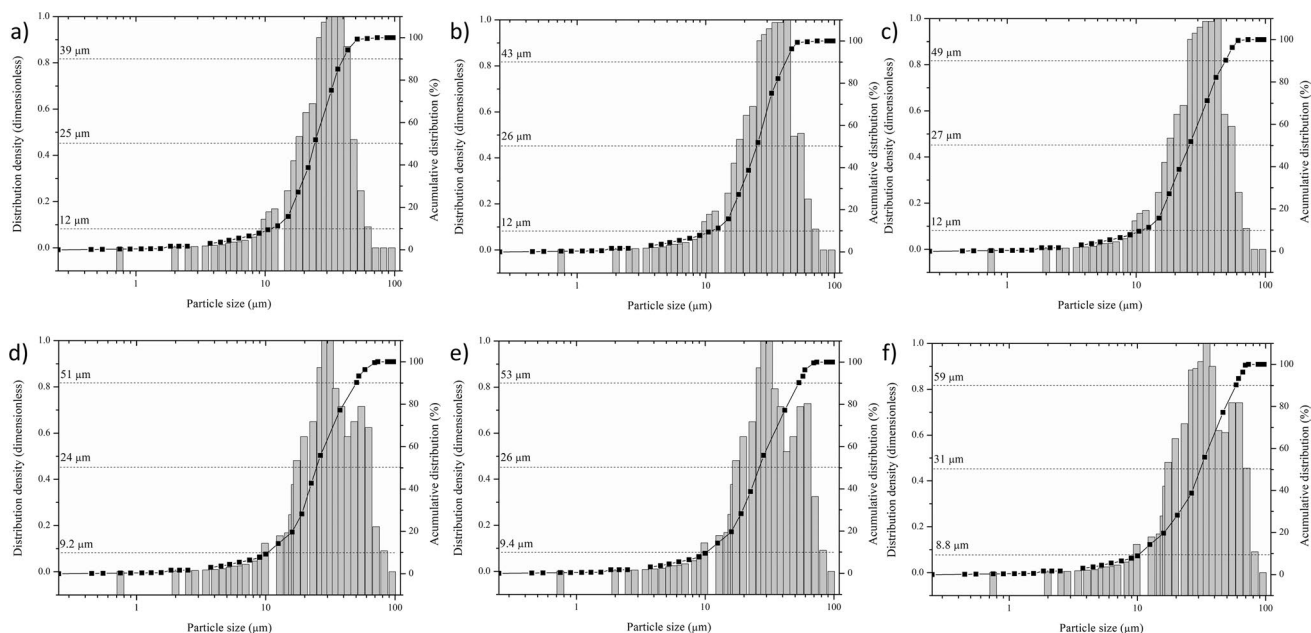
Fig. 5 Particle size distribution of **a** HAp-10wt.%PS, **b** HAp-20wt.%PS, **c** HAp-30wt.%PS powder mixtures prepared by roll milling during 2h, and **d** HAp-10wt.%PS, **e** HAp-20wt.%PS, **f** HAp-30wt.%PS powder mixtures prepared by roll milling during 4h
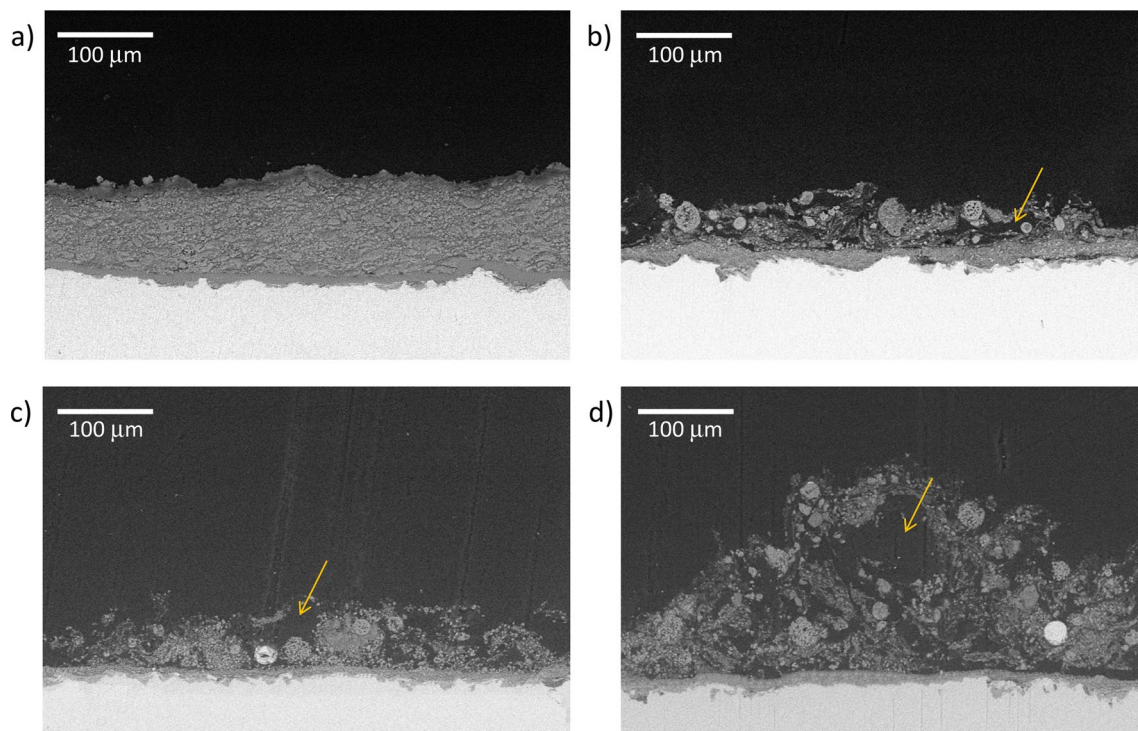
Fig. 6 SEM images of the cross-section of **a** HAp coating (H0); **b** HAp-10wt.%PS coating (H1), **c** HAp-20wt.%PS coating (H2), **d** HAp-30wt.%PS coating (H3)

polymeric material upon impact. The typical lamellar structure of HAp coatings obtained by HVOF was also observed in these coatings.

The average coating thickness and percentage of PS calculated in the cross-sectional area of the as-sprayed coatings are presented in Fig. 7a. The thickness obtained for the H0 coating (110 µm) is included as a reference value. When adding 10 wt.% and 20 wt.%. PS, a reduction in coating thickness is observed, with values of 66 µm and 72 µm for the H1 and H2 coatings, respectively. Interestingly, the coating thickness increases again to a value of 180 µm in the H3 coating when the PS percentage is increased to 30 wt.%. The H3 coating shows non-uniform thickness though, as indicated by the standard deviation bar in Fig. 7a. Previous studies [44, 48–50] have reported that factors such as particle size distribution, the difference in thermal conductivity
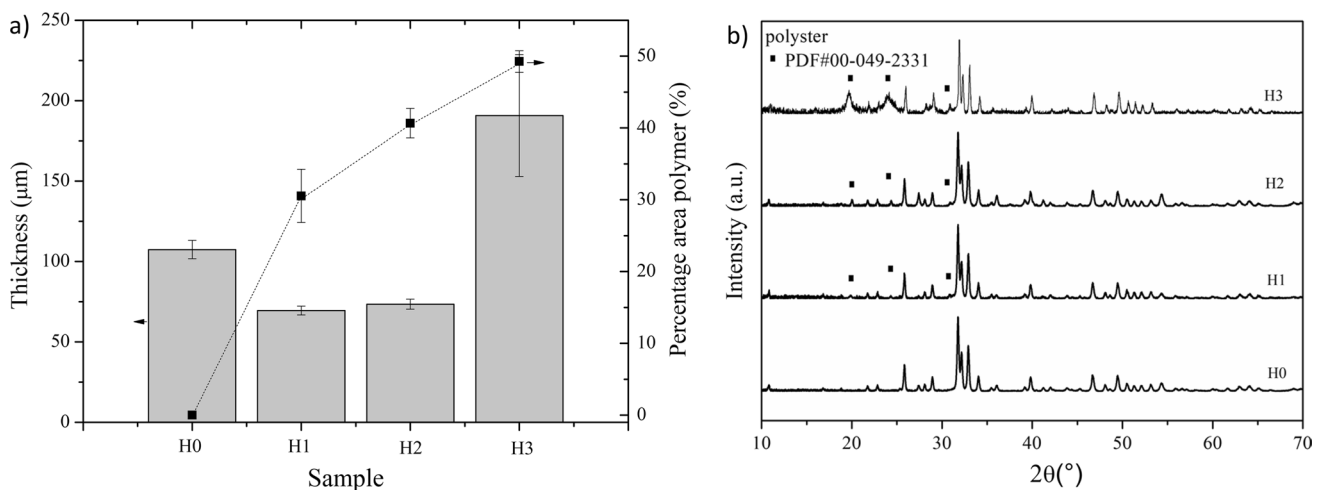
Fig. 7 **a** Thickness and percentage area of polymer and **b** XRD patterns of the HAp-PS coatings (H0, H1, H2, H3) prepared by HVOF

between the added material and the matrix, and the amount of the secondary phase added play a crucial role in either decreasing or increasing coating thickness in thermally sprayed mixtures. In the present study, the reduction in coating thickness for H1 and H2 samples compared to H0 can be attributed to the variation in thermal energy conditions experienced by the HAp powder due to the presence of PS. Part of the energy generated by the flame in the HVOF process is required to melt both materials, thereby modifying the melting state of the HAp particles during impact [51]. In fact, the cross-sectional images of the coatings in Fig. 6b, c show the presence of some unmolten HAp particles in the obtained coatings. On the other hand, the increase in thickness of the H3 coating could be attributed to the higher amount of polymer and the larger size of the agglomerates present in the feedstock powder. Under these conditions, less thermal degradation of the in-flight PS particles, acting as a ductile phase to retain HAp particles during impact, may occur. Moreover, Fig. 6d shows the presence of larger areas associated with PS (yellow arrow) compared to those observed in the H2 and H1 coatings. Similar results have been reported in previous works on HVOF-sprayed coatings employing polymeric PET powders [52].

In this work, the surface roughness of the as-sprayed coatings was also measured presenting values of 4.96 ± 0.51 μm, 4.76 ± 0.54 μm, 4.81 ± 0.49 μm, and 5.31 ± 0.45 μm for the HAp, HAp-10%PS, HAp-20%PS, and HAp-30%PS, respectively. Overall, thermal sprayed coatings tend to copy the roughness pattern of the substrate. Substrate roughness is crucial for the deposition of molten particles at impact since it is required during the solidification of particles upon impact to ensure mechanical anchoring. The recommended substrate roughness value in thermal spraying is about 5 μm. In this work, the experimental roughness value of the substrate surface was 5.02 ± 0.41 μm. Then, the results confirm that the coating's roughness is similar to that of the substrate.

It is noteworthy that all the investigated coatings in this study were deposited onto a TiO_2 bond coat layer. The TiO_2 bond coat exhibited an average thickness of 14.7 μm $\pm$ 5.4 μm and an average porosity of $1.2\% \pm 0.4\%$ across all samples. These findings are consistent with prior studies [19, 20] involving the fabrication of TiO_2 bond coat coatings by HVOF on titanium alloys, employing powders with similar phases and particle sizes as those utilized in the present research. It is well-established [19] that during the fabrication of TiO_2 bond coats by HVOF, a transformation of the Magnelli and anatase phases occurs, resulting in coatings predominantly composed of the rutile phase due to the elevated temperatures and oxidizing atmospheres experienced by the particles in the process.

Figure 7b presents the results of XRD analyses of the H0, H1, H2, and H3 coatings obtained by HVOF. The results reveal the presence of diffraction peaks associated with crystalline HAp in all coatings. In addition, diffraction peaks associated with poly(p-benzoate) (PS) appear in the H1, H2, and H3 coatings confirming its presence in these coatings. The intensity of the diffraction peaks associated with poly(p-benzoate) increases as the percentage of PS added to the coatings is higher. Notably, there is a variation in the lattice parameters and cell volume of HAp in some of the obtained coatings compared to those of the feedstock HAp powder, as shown in Table 2. Initially, for the H0 coating, a contraction of the c-parameter and a decrease in the total cell volume are observed compared to the starting HAp powder. These lattice parameter variations are also observed to a lesser extent in the H1 and H2 coatings, while no significant changes are found for the H3 coating. Previously reported works in the literature [53] have associated the variation in the c-parameter of HAp with changes in the content of OH^- vacancies in its crystal structure due to melting and solidification of the HAp particles during thermal spray processes.

The interfacial adhesion of the H0, H1, and H2 coatings without exposure to SBF, was obtained by performing Vickers indentations at the TiO_2-HAp interface and following a procedure reported by Henao et al. [19]. This property was measured at the TiO_2/HAp interface because the porous HAp-PS coatings are directly adhered to the TiO_2 layer and not to the Ti-6Al-4V substrate. The interfacial adhesion values for the H0, H1, and H2 coatings were 1.160, 1.169, and 1.184 MPa/m$^{1/2}$, respectively. The adhesion value reported for a dense HAp coating produced by HVOF on a Ti-6Al-4 V substrate is 1.159 MPa/m$^{1/2}$ [19]. Hence, the bonding strength values reported for the HAp-PS coatings produced in this research are comparable to those found in dense HAp counterparts produced by HVOF thermal spraying.

Figure 8a presents the results of the thermogravimetric analysis conducted on the PS powder. The analysis reveals a single-stage degradation, which is typical for polyesters [54]. The onset of degradation occurs around 266 °C and is completed at 600 °C. This result served as a basis for conducting post-thermal treatments on the H1 and H2 coatings to remove the PS, which was employed in this study as the porosity-forming phase. As already outlined, the H3 coating was not considered for further treatment due to its non-uniform thickness and the presence of large

Table 2 Structural parameters of the coatings

| Sample	$a = b$ (Å)	c (Å)	Volume (Å^3)	χ^2
HAp powder	9.425 ± 0.001	6.875 ± 0.001	528.87	1.97
H0	9.426 ± 0.001	6.859 ± 0.001	527.76	2.20
H1	9.425 ± 0.001	6.862 ± 0.001	527.87	2.01
H2	9.425 ± 0.001	6.870 ± 0.001	528.49	1.78
H3	9.425 ± 0.001	6.875 ± 0.001	528.87	1.98
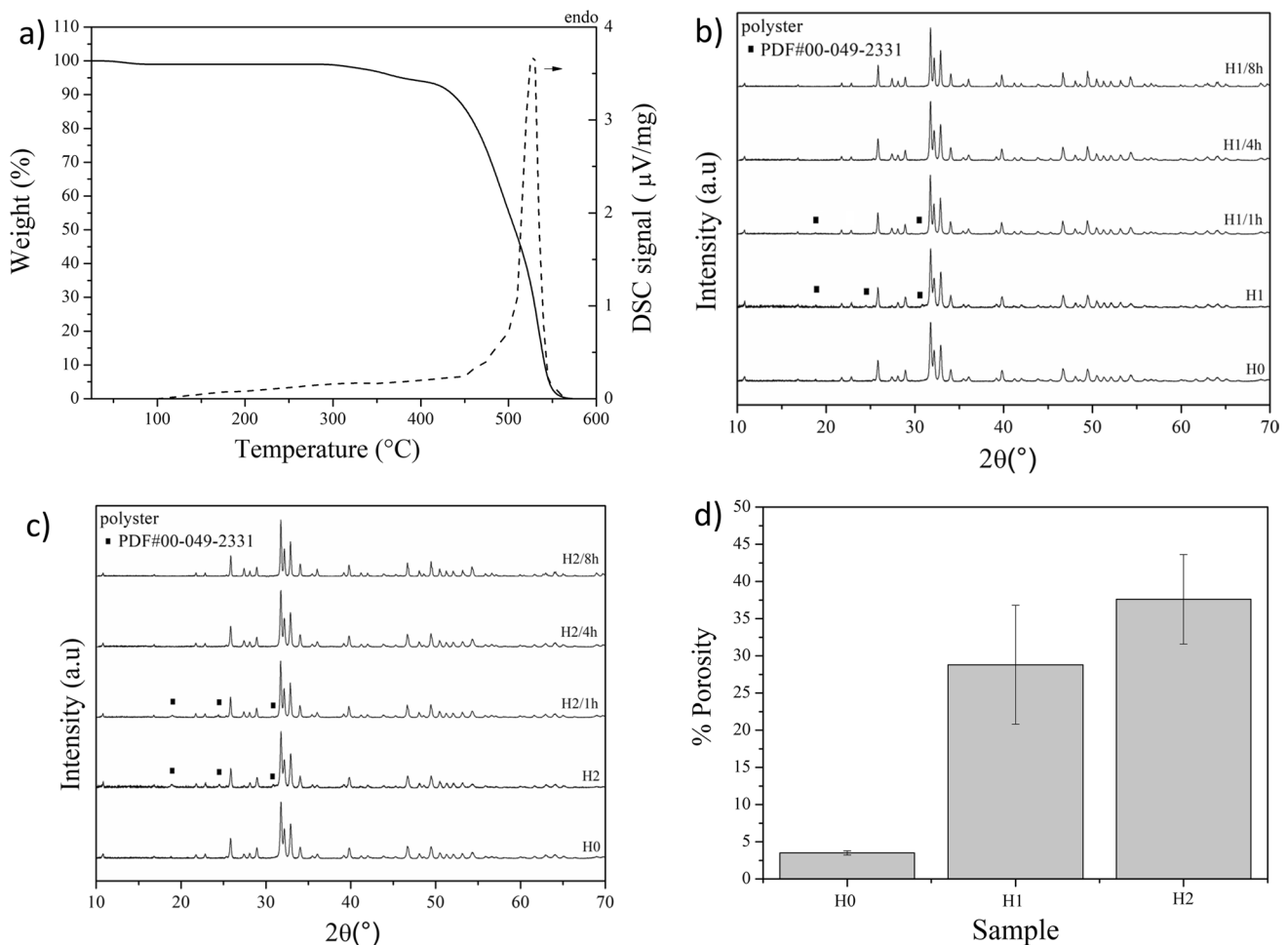
Fig. 8 Results of **a** TGA analysis of the PS powder, **b** XRD analysis of the H1 coating, **c** XRD analysis of the H2 coating before and after the thermo-chemical treatment, and **d** porosity level of the coatings after the thermochemical treatment

agglomerates, which posed a risk to its mechanical stability. All thermal treatments were carried out at 600 °C for 1 h, 4 h, and 8 h. Subsequently, a xylene wash was performed, as xylene is commonly used as a solvent for polyesters [55], to remove any possible remaining organic components after the thermal treatment of the coatings.

Figure 8b, c shows the results of the XRD analyses of the H1 and H2 coatings after thermal treatment. The results indicate that both H1 and H2 coatings exhibit diffraction peaks related to residual PS after 1 h thermal treatment. However, the results reveal that it was possible to completely remove the PS from the H1 and H2 coatings after a 4 h thermal treatment. The presence of residual PS at 1 h of treatment may be attributed to incomplete thermal degradation of the PS volume present in the samples. In fact, studies conducted with the same porosity-forming phase in plasma sprayed coatings have also reported complete removal of PS after only 1 h of thermal treatment, even in 1 mm-thick coatings [56].

Figure 8d shows the results of the porosity analysis of the coatings after removing the porosity-forming phase. The results obtained for the H1 and H2 coatings are compared with the H0 coating, which had a porosity value of 3.8%. The use of the porosity-forming phase allows for an increase in the porosity of the HAp coatings, with average values of 27% and 38% for the H1 and H2 coatings, respectively. No statistical difference in the porosity levels achieved for H1 and H2 coatings is observed. In addition, Fig. 9 provides a comparison of the surface of H0, H1, and H2 coatings studied by optical microscopy. The results show the appearance of visible surface pores in the H1 and H2 coatings after removing the porosity-forming phase (indicated by yellow arrows in Fig. 9b, c). In the optical profilometry images (Fig. 9d, e, and f), a change in the valley profile is observed for the H1 and H2 samples compared with the H0 sample. The blue regions in the color scale of the optical profilometry images are associated with areas of greater depth, corresponding to regions where the internal porosity
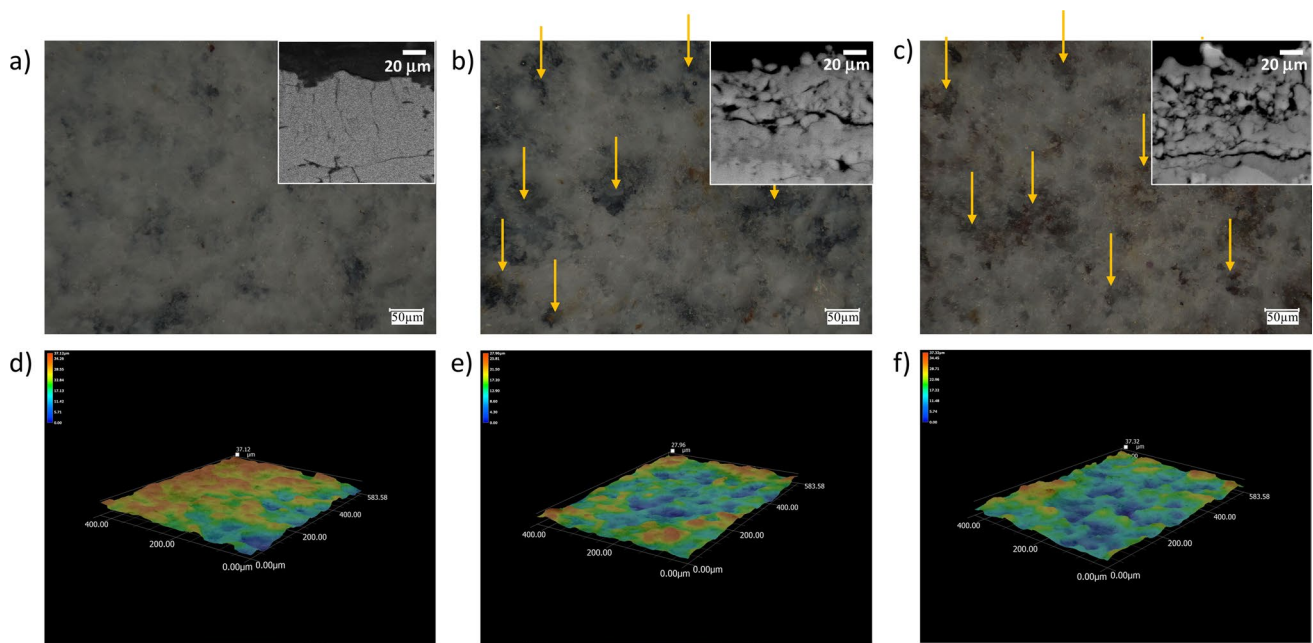
Fig. 9 Optical micrographs on the top surface of the HAp-PS coatings after thermo-chemical treatment **a** H0 coating, **b** H1 coating and **c** H2 coating

connects with the surface of the coating. As a result, the surface roughness of the H1 and H2 coatings slightly changes if compared with the as-sprayed HAp coating, presenting values of 5.71 ± 0.42 µm and 5.94 ± 0.53 µm, respectively. In addition, the insets in Fig. 9a, b, and c show the cross-sectional views of the H0, H1, and H2 coatings, respectively, illustrating the increase in porosity induced by the removal of the porosity-forming phase.

Previous studies employing mullite and PS as a porosity-forming agent in plasma sprayed coatings [56] have also reported an increase of porosity up to 79%. In this work, a maximum porosity of 38% was attained using the HVOF technique and HAp-PS powder mixtures. Notably, HVOF offers advantages over plasma spray for producing HAp coatings for biomedical applications, particularly due to the observed crystallinity in the HAp coatings prepared by HVOF. Over prolonged interaction with body fluids, HAp coatings manufactured by HVOF demonstrate enhanced mechanical stability and bone promotion compared to plasma sprayed counterparts with higher metastable phase content [17, 35]. In this regard, this study opens the possibility of exploring HVOF-sprayed HAp porous coating architectures, produced employing a PS porosity-forming phase, to analyze cellular proliferation and adhesion with the aim of visualizing a wider biological response that shed light for future in-vivo applications.

In this study, as an initial approach to investigate the biological response of the porous HAp coatings obtained by HVOF, in-vitro electrochemical tests were performed in SBF. Figures 10, 11, and 12 present the results of the electrochemical characterization for the H0, H1, and H2 coatings evaluated in Hank's solution for 28 days. Figure 10a, b shows the Nyquist and Bode plots for the H0 coating. Incomplete semicircles with varying curvature radii are observed, corresponding to changes in impedance with immersion time in SBF. The inset in Fig. 10a reveals the formation of semicircles with diameters ranging from 0 to 250 Ω/cm^2, varying with immersion time. These semicircles are typically observed in HAp coatings immersed in SBF and are associated with the apatite formation process on the coating surface, known as maturation, involving ion exchange between the SBF and the solid hydroxyapatite phase [20]. The present study confirmed the formation of such apatite layer after 28 days of immersion (see supplementary material). The Bode plot shows certain stability in impedance values at low frequencies, while at higher frequencies (> 1000 Hz), impedance values exhibit some variations. Variations in impedance values at higher frequencies (> 1000 Hz) are known to be associated with contributions from electrolyte resistance [57]. In fact, for the H0 coating, an increase in impedance values at higher frequencies is observed from day 1 of immersion, reaching its maximum at day 14, suggesting changes in Ca^{2+} and PO_4^{3-} ion content in the solution, involved in the ion exchange between the HAp coating and SBF to form apatite. The Bode plot confirms the observations from the Nyquist curve, suggesting that after 14 days, a certain stability is achieved in the formation of the apatite layer on the HVOF-sprayed HAp coating.
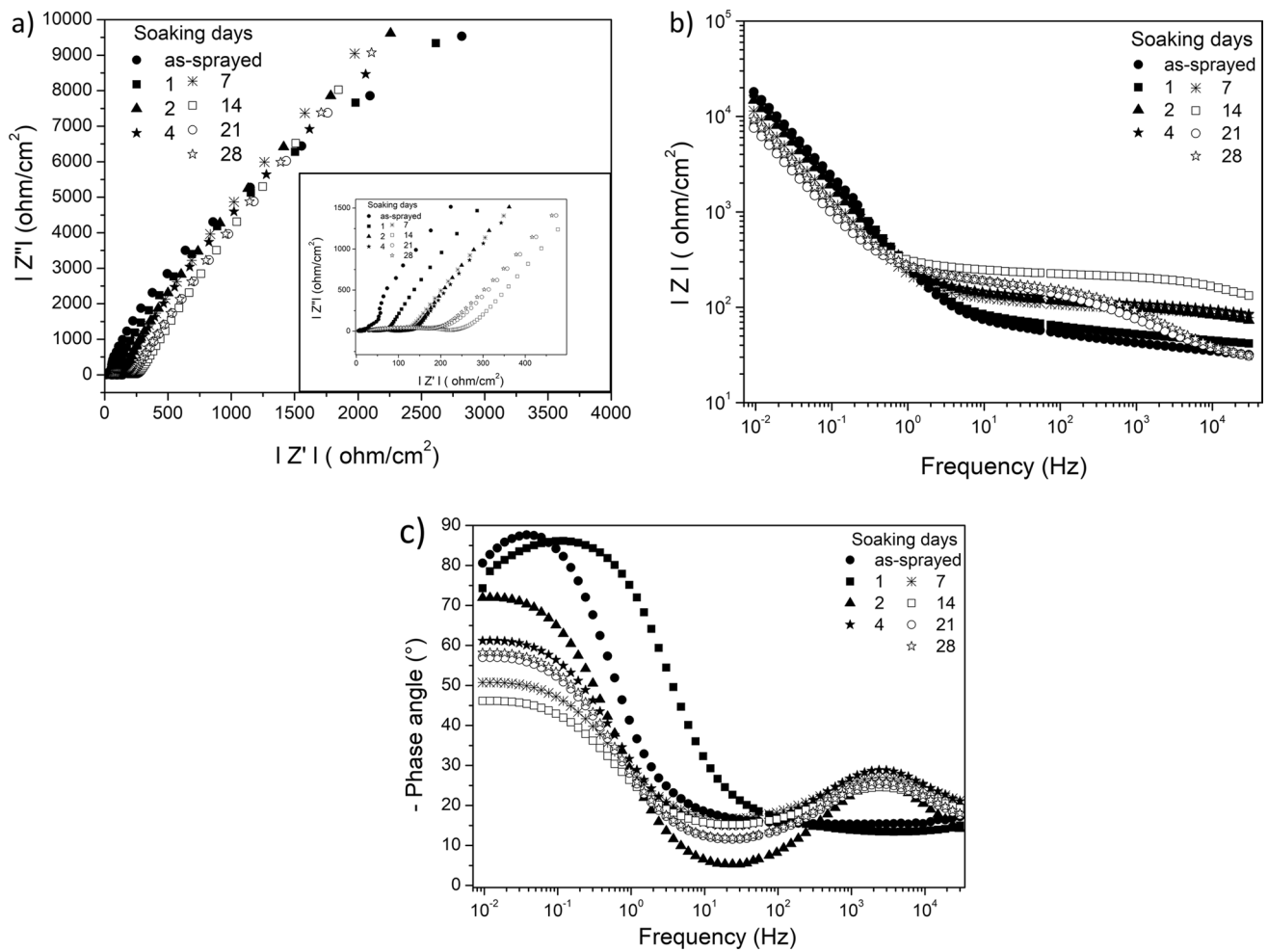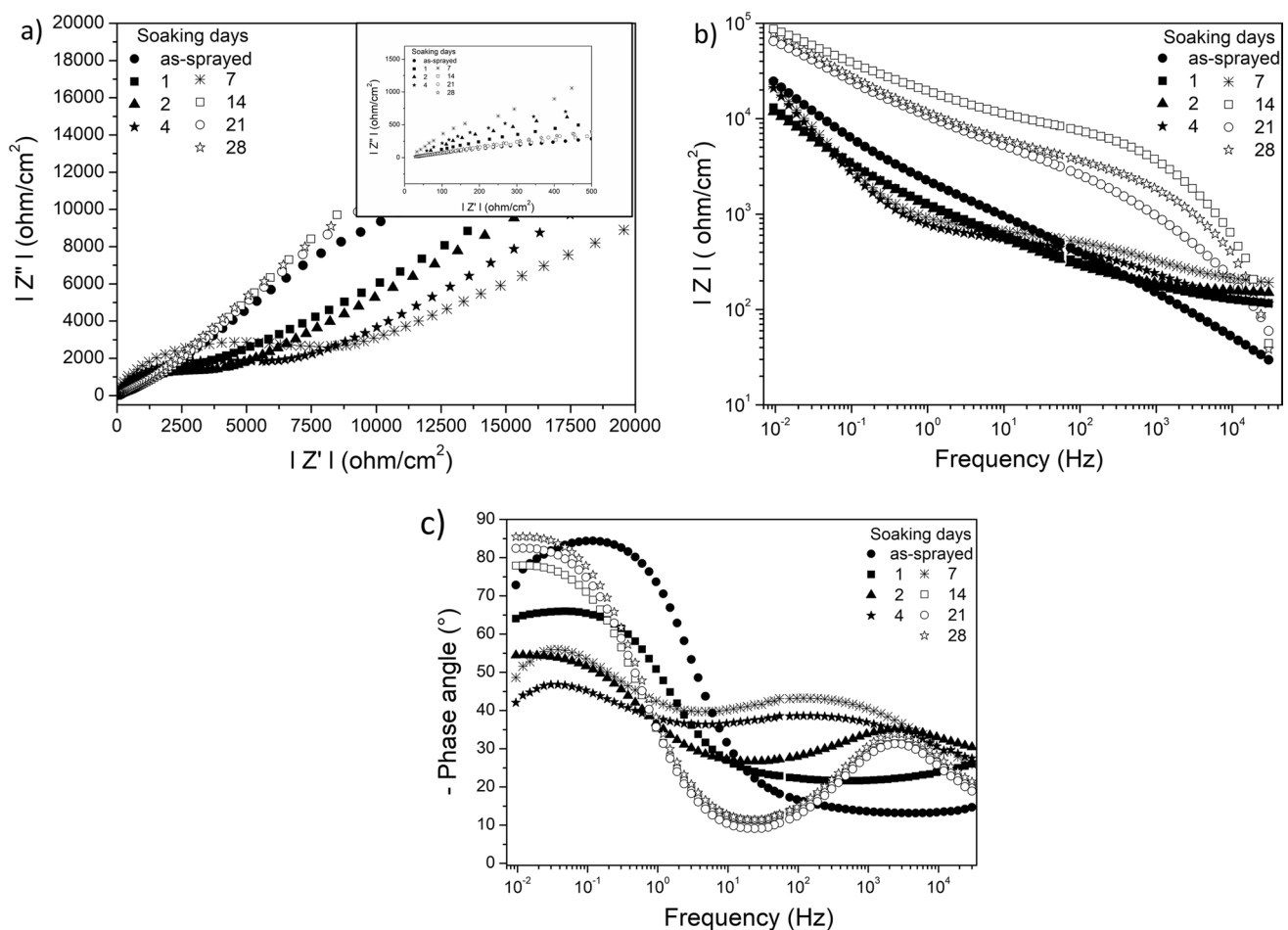
Fig. 10 EIS plots for the hydroxyapatite coating (H0) obtained by HVOF and immersed for 28 days in SBF at 37 °C. **a** Nyquist plot, **b** Bode diagram, **c** phase angle vs frequency plot

The capacitive behavior of the H0 coating is further supported by the phase angle plot shown in Fig. 10c. This result shows the formation of a time constant during the initial hours of immersion (0–24 h) and the appearance of a second time constant at high frequencies (10^3–10^4 Hz) from day 2 of immersion in the SBF. Phase angles approximating -80° result from the capacitive behavior of the HAp coating at the beginning of the immersion test, while the lower angles are attributed to diffusion processes between the electrolyte and the solid phase of the coating, associated with the formation of apatite on the surface [20, 58]. This finding suggests that the diffusion process associated with apatite formation reaches its maximum between 7 and 14 days of coating immersion, resulting in an angle close to $-45°$. This agrees with the results included in the Bode plot, where a reduction in the impedance value at high frequency ($> 10^3$ Hz) is observed after 14 days of immersion. Despite this decrease, diffusion processes are still observed (angles between $-55°$ and $-60°$), possibly due to ongoing apatite formation on the

exposed surface of the HAp coating through the characteristic cracks in the apatite layer (see supplementary material).

Figure 11a shows the Nyquist plot for the H1 coating evaluated in Hank's solution over a period of 28 days. Interestingly, the H1 coating exhibits the formation of two incomplete semicircles between 1 and 7 days of immersion in SBF. In addition, a single incomplete semicircle is observed for the sample evaluated between 14 and 28 days. This result suggests, as discussed for the H0 coating, that the bone-like apatite formation process occurs during the first 7 days of immersion in SBF, reaching the largest diameter of the incomplete semicircle, associated with the apatite formation process, a value of 8700 Ω/cm^2. The Bode plot in Fig. 11b for the H1 coating shows a similar behavior of impedance at low frequency between 1 and 7 days of immersion. Furthermore, an increase in impedance at low frequency is observed for the coating evaluated between 14 and 28 days. As also observed in the H0 coating, there is a variation in impedance at high frequency ($> 10^3$ Hz), which is associated with
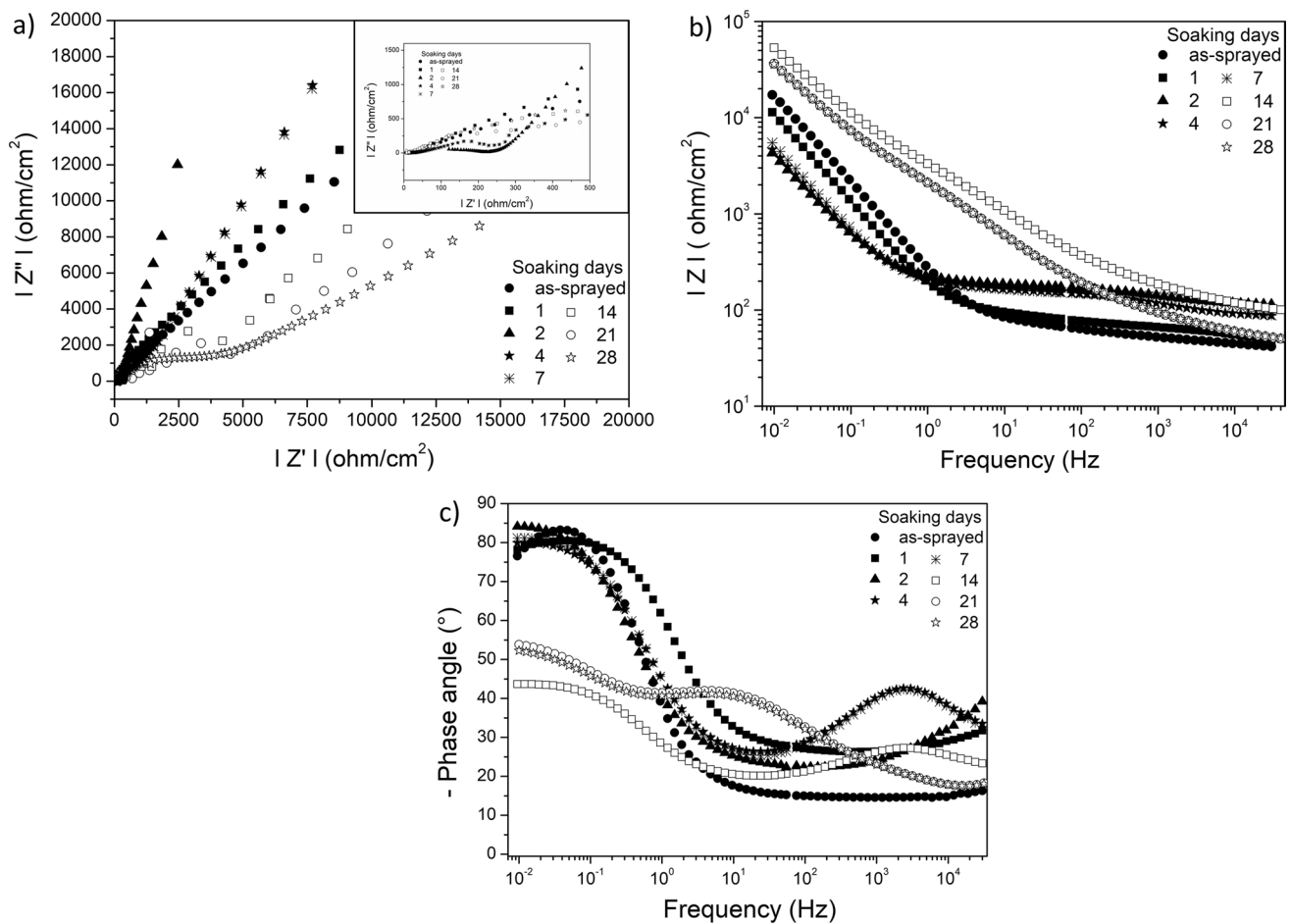
Fig. 11 EIS plots for the porous hydroxyapatite coating (H1) obtained by HVOF and immersed for 28 days in SBF at 37 °C. **a** Nyquist plot, **b** Bode diagram, **c** phase angle vs frequency plot

the ionic interaction process between the electrolyte and the HAp coating, resulting in the formation of the apatite layer. Interestingly, for the H1 coating evaluated between 14 and 28 days, a significant drop in impedance at high frequencies ($> 10^3$ Hz) is observed, accompanied by an increase in impedance at low frequency (< 0.1 Hz) compared to the coatings evaluated between 1 and 7 days of immersion. This behavior may be associated with the decrease in surface ionic activity, resulting in the formation of bone-like apatite layer and a more resistive coating. Previous studies on porous HAp coatings fabricated by electrophoresis have also reported an increase in impedance after prolonged immersion in Hank's solution, attributing this behavior to the stability of the apatite layer formed due to the interaction between the porous coating and the SBF [59].

In addition, the phase angle plot as a function of frequency for the H1 coating (Fig. 11c) shows the appearance of two-time constants between day 1 and day 28 of immersion in SBF. This result is similar to that observed for the H0 coating regarding the apatite formation. Interestingly,

the formation of two-time constants and angles close to -80° confirms the capacitive behavior of the H1 coating once the bone-like apatite formation is stabilized on the coating's surface. The greater stability of the H1 coating compared to H0 suggests a possible decrease in active sites associated with the ionic interaction between the hydroxyapatite phase and the electrolyte in the H1 coating, which can be attributed to the presence of porosity and the formation of apatite within these pores. In contrast, the H0 coating exhibits a higher dependence on the formation of cracks in the apatite layer, promoting the penetration of the solution through them, leaving a larger exposed volume for new interactions between the electrolyte and the hydroxyapatite phase. As seen in the Bode plot and phase angle of the H1 coating, although there is better protection of the coating, the presence of a second time constant and the decrease in impedance values at high frequency do not suggest a complete absence of ionic interaction but rather a reduction in the interaction with the ionic species.

Fig. 12 EIS plots for the porous hydroxyapatite coating (H2) obtained by HVOF and immersed for 28 days in SBF at 37 °C. **a** Nyquist plot, **b** Bode diagram, **c** phase angle vs frequency plot

Figure 12a shows the Nyquist plot for the H2 coating. The Nyquist plot for the initial state and the first day of testing exhibits the formation of an incomplete semicircle associated with capacitive behavior of the coating. In addition, the appearance of a first incomplete semicircle with a range of 0–250 Ω/cm^2 is observed between 2 and 7 days of immersion in SBF, which also suggests the formation of apatite during immersion as it was also observed in the H0 coating. Subsequently, an increase in the diameter of the first incomplete semicircle is observed between 14 and 28 days, ranging between 2500 and 5000 Ω/cm^2, while the larger second incomplete semicircle also increases its curvature, indicating a capacitive behavior. On the other hand, the Bode plot for the H2 coating in Fig. 12b shows a similar behavior in impedance at low frequencies (< 0.1 Hz), with a decrease in impedance for tests conducted between 2 and 7 day immersion, and an increase between 14 and 28 days. Previous studies have also reported an increase in impedance at low frequencies on porous surfaces between 21 and 28 day immersion for in-vitro cellular tests, which is related

to the reduction in the available surface area for the corrosion process of the sample in contact with body fluid due to the adhesion and proliferation of preosteoblasts [60]. In the present study, although there are no cells present, it is suggested that the observed increase in impedance between 14 and 28 day immersion in the H2 coating may be associated with the blocking of active sites due to the formation of bone-like apatite, both on the surface and within the available porosity in the coating. In addition, variation in impedance at high frequency (> 1000 Hz) is observed, confirming the interaction between the coating and the electrolyte, leading to the formation of apatite. This variation is more pronounced between 2 and 14 day immersion, with a greater increase in impedance at high frequency. The observations in the Bode plot are complemented by the phase angle plot in Fig. 12c, where a time constant is observed in the early hours of immersion (between 0 and 1 day), and the appearance of a second time constant at high frequencies for samples analyzed between 2 and 28 day immersion. Specifically, the second time constant appears on day 2 at frequencies greater

than 10^3 Hz whereas for immersion times between 4 and 14 days the constant is defined in the range between 10^2 and 10^4 Hz. In addition, there is a displacement to intermediate frequencies (10^1 and 10^2 Hz) for days 21 and 28 immersion. The phase angles tending to $-45°$ also suggest the occurrence of diffusive processes associated with apatite formation, as observed in the H0 and H1 coatings. In this case, unlike the H0 coating, the apatite layer seems to consolidate between 14 and 28 days (i.e., phase angles closest to $-45°$ are observed). However, no angles close to $-80°$ are registered in H2 coating, indicating a lack of stabilization of the bone-like apatite layer after 28 days.

4 Conclusions

In this study, a method for manufacturing porous hydroxyapatite-based coatings by HVOF spray using a second porogen phase was investigated. The chosen porous-forming phase was polyester, a polymeric material that degrades upon heat treatment, promoting the formation of pores in the coating. Different weight percentages (ranging from 10 to 30 wt.%) of polyester were mixed with hydroxyapatite, and optimal mixing parameters were identified to achieve the required fluidity for successful HVOF spraying. The fabrication of composite coatings containing hydroxyapatite and polyester by HVOF was successfully demonstrated. For the fabrication of the HAp-PS composite coatings, previously optimized parameters for spraying of pure hydroxyapatite coatings were employed. The incorporation of the porous-forming phase significantly increases the porosity of the hydroxyapatite coating, raising it from 3.8% in a HVOF-sprayed pure HAp coating up to 38% in HAp-20wt.%PS HVOF-sprayed counterparts, once the porogen phase is removed. This methodology opens the possibility for future research to explore coatings with different degrees of porosity and porous HAp architectures for potential biomedical applications; particularly, focusing on biological performance such as bone in-growth promotion, cellular proliferation, and adhesion.

In this study, a preliminary in-vitro investigation of the behavior of a porous HVOF-sprayed hydroxyapatite coating with porosities of 28% and 38% was conducted using electrochemical techniques in simulated body fluid at 37 °C. The results revealed that the electrochemical response of the porous coatings differs to that found in the dense hydroxyapatite coating. All coatings showed ionic interaction and diffusion phenomena, resulting in the formation of a bone-like apatite layer. However, the process slowed down or stabilized differently in each type of coating due to the variation in the coating's surface area and volume, as a result of the different porosity levels studied here. The electrochemical results indicate that the penetration of simulated body fluid generates different impedance responses in the porous coatings, leading to apatite formation. The decrease in active sites in the porous coatings after prolonged immersion potentially suggests the occurrence of bone-in-growth phenomena. This finding provides a starting point for further detailed studies on bone-in-growth occurring in HVOF-produced porous hydroxyapatite coatings.

References

1. J.M. Haglin, A.E.M. Eltorai, J.A. Gil, S.E. Marcaccio, J. Botero-Hincapie, A.H. Daniels, Orthop. Surg.. Surg. **8**, 417 (2016)
2. W. Jin, P.K. Chu, *Orthopedic Implants* (Elsevier Inc, 2019)
3. J.T. Evans, J.P. Evans, R.W. Walker, A.W. Blom, M.R. Whitehouse, A. Sayers, Lancet (London, England) **393**, 647 (2019)
4. A. Amini, J. Wallace, S. Nukavarapu, J Long Term Eff. Med. Implant. **21**, 93 (2011)
5. M.R. Streit, M.M. Innmann, C. Merle, T. Bruckner, P.R. Aldinger, T. Gotterbarm, Clin. Orthop. Relat. Res.. Orthop. Relat. Res. **471**, 3262 (2013)
6. J. Otomo-Corgel, J.J. Pucher, M.P. Rethman, M.A. Reynolds, J. Evid. Based Dent. Pract.Evid. Based Dent. Pract. **12**, 20 (2012)
7. Y.M.K. Baghdadi, A.N. Larson, R.J. Sierra, Clin. Orthop. Relat. Res.. Orthop. Relat. Res. **471**, 3251 (2013)
8. G. Bergmann, A. Bender, J. Dymke, G. Duda, P. Damm, PLoS ONE **11**, 1 (2016)
9. R. Meldrum, L. Wurtz, J. Feinberg, W. Capello, Iowa Orthop. J.Orthop. J. **25**, 17 (2004)
10. F.D. Al-Shalawi, A.H. Mohamed Ariff, D.W. Jung, M.K.A. Mohd Ariffin, C.L. Seng Kim, D. Brabazon, M.O. Al-Osaimi, Polymers (Basel) **15**, 2601 (2023)
11. W.N. Capello, J.A. D'Antonio, J.R. Feinberg, M.T. Manley, J. Bone Jt. Surg. **79**, 1023 (1997)

12. H. Singh, R. Kumar, C. Prakash, S. Singh, Mater. Today Proc. **50**, 612 (2021)

13. A. Binahmed, A. Stoykewych, A. Hussain, B. Love, V. Pruthi, Int. J. Oral Maxillofac. Implant **22**, 963 (2007)

14. J.H. Jung, S.Y. Kim, Y.J. Yi, B.K. Lee, Y.K. Kim, J. Adv. Prosthodont. **10**, 85 (2018)

15. T.T. Li, L. Ling, M.C. Lin, H.K. Peng, H.T. Ren, C.W. Lou, J.H. Lin, J. Mater. Sci. **55**, 6352 (2020)

16. L. Sun, C.C. Berndt, K.A. Gross, A. Kucuk, J. Biomed. Mater. Res. **58**, 570 (2001)

17. A.M. Vilardell, N. Cinca, N. Garcia-Giralt, S. Dosta, I.G. Cano, X. Nogués, J.M. Guilemany, Mater. Sci. Eng. C **107**, 110306 (2020)

18. R. Kumari, J.D. Majumdar, Mater CharactCharact. **131**, 12 (2017)

19. J. Henao, M. Cruz-Bautista, J. Hincapie-Bedoya, B. Ortega-Bautista, J. Corona-Castuera, A.L. Giraldo-Betancur, D.G. Espinosa-Arbeláez, J.M. Alvarado-Orozco, G.A. Clavijo-Mejía, L.G. Trapaga-Martínez, C.A. Poblano-Salas, J. Therm. Spray Technol. **27**, 1302 (2018)

20. J. Henao, O. Sotelo-Mazon, A.L. Giraldo-Betancur, J. Hincapie-Bedoya, D.G. Espinosa-Arbelaez, C. Poblano-Salas, C. Cuevas-Arteaga, J. Corona-Castuera, L. Martinez-Gomez, J. Mater. Res. Technol. **9**, 14002 (2020)

21. J.A. Hermann-Muñoz, J.A. Rincón-López, G.A. Clavijo-Mejía, A.L. Giraldo-Betancur, J.M. Alvarado-Orozco, A. De Vizcaya-Ruiz, J. Muñoz-Saldaña, Surf. Coat. Technol. **358**, 299 (2019)

22. K.W. Widantha, E.A. Basuki, E. Martides, B. Prawara, J. Biomater. Appl.Biomater. Appl. **36**, 375 (2021)

23. A. Unnanuntana, B.J. Rebolledo, M. Michael Khair, E.F. Dicarlo, J.M. Lane, Clin. Orthop. Relat. Res.. Orthop. Relat. Res. **469**, 2194 (2011)

24. T.T. Li, Y. Zhang, H.T. Ren, H.K. Peng, C.W. Lou, J.H. Lin, Carbohydr. Polym.. Polym. **260**, 1 (2021)

25. A.M. Yousefi, J. Appl. Biomater. Funct. Mater. **17**, 55 (2019)

26. B.G.X. Zhang, D.E. Myers, G.G. Wallace, M. Brandt, P.F.M. Choong, Int. J. Mol. Sci. **15**, 11878 (2014)

27. V. Karageorgiou, D. Kaplan, Biomaterials **26**, 5474 (2005)

28. L. Yu, T.M. Silva-Santisteban, Q. Liu, C. Hu, J. Bi, M. Wei, J. Biomed. Mater. Res. Part A **109**, 615 (2021)

29. J. Wang, P. Layrolle, M. Stigter, K. De Groot, Biomaterials **25**, 583 (2004)

30. Y.C. Liu, G.S. Lin, Y. Te Lee, T.C. Huang, T.W. Chang, Y.W. Chen, B.S. Lee, K.L. Tung, Surf. Coat. Technol. **393**, 125837 (2020)

31. A. Buanz, *Remington. The Science and Practice of Pharmacy* (Elsevier, 2021), p.295

32. M. Li, P.D. Christofides, Chem. Eng. Sci. **60**, 3649 (2005)

33. H. Kurzweg, R.B. Heimann, T. Troczynski, J. Mater. Sci. Mater. Med. **9**, 9 (1998)

34. G.A. Clavijo-Mejía, D.G. Espinosa-Arbeláez, J.A. Hermann-Muñoz, A.L. Giraldo-Betancur, J. Muñoz-Saldaña, J. Therm. Spray Technol. **28**, 1160 (2019)

35. C.C. Berndt, F. Hasan, U. Tietz, K.-P. Schmitz, in *Advances in Calcium Phosphate Biomaterials*. ed. by B. Ben-Nissan (Springer, 2014), pp.267–329

36. J.W. Nicholson, J. Am. Chem. Soc. **125**, 850 (2003)

37. A. Yamakata, J.J.M. Vequizo, J. Photochem. Photobiol. C Photochem. Rev. **40**, 234 (2019)

38. P.I. Gouma, M.J. Mills, J. Am. Ceram. Soc. **84**, 619 (2001)

39. S. Sangeetha, S. R. Kathyayini, P. D. Raj, P. Dhivya, and M. Sridharan, Proc. Int. Conf. "Advanced Nanomater. Emerg. Eng. Technol. ICANMEET 2013 404 (2013)

40. M. Canillas, A. Rajnicek, C. Rosero, E. Chinarro, B. Moreno, Key Eng. Mater. **493–494**, 896 (2012)

41. F.C. Walsh, R.G.A. Wills, Electrochim. Acta. Acta **55**, 6342 (2010)

42. S. Sreeja, C.V. Muraleedharan, P.R.H. Varma, G.S. Sailaja, Mater. Sci. Eng. C **109**, 110491 (2020)

43. https://polymerdatabase.com/Polymer/classes/Polyarylate/type.Html 2023 (2023)

44. M. Robotti, S. Dosta, I.G. Cano, A. Concustell, N. Cinca, J.M. Guilemany, Adv. Powder Technol. **27**, 1257 (2016)

45. J. Henao, C.A. Poblano-Salas, F. Vargas, A.L. Giraldo-Betancur, J. Corona-Castuera, O. Sotelo-Mazón, *Advanced Surface Coating Techniques for Modern Industrial Applications* (IGI Global, 2020), pp.31–70

46. L. Legoix, C. Gatumel, M. Milhé, H. Berthiaux, V. Mizonov, Chem. Eng. Res. Des. **121**, 1 (2017)

47. H. Katanoda, S. Kuroda, J. Kawakita, K. Fukanuma, K. Matsuo, Proc. Int. Therm. Spray Conf. **525**, 146 (2004)

48. C. Mateus, S. Costil, R. Bolot, C. Coddet, Surf. Coatings Technol. **191**, 108 (2005)

49. G. Martinez, J. Henao, V. Mandujano-González, A. Giraldo-Betancur, P.A. Forero-Sossa, J. Corona-Castuera, M.A. Rivera-Gil, C. Poblano-Salas, Appl. Phys. A Mater. Sci. Process. **128**, 1 (2022)

50. M. Ivosevic, R.A. Cairncross, R. Knight, Proc. Int. Therm. Spray Conf. **790**, 84 (2004)

51. D. Lisjak, P. Lintunen, A. Hujanen, T. Varis, G. Bolelli, L. Lusvarghi, M. Jagodič, M. Drofenik, Mater. Lett. **65**, 534 (2011)

52. H. Koivuluoto, J. Therm. Spray Technol. **31**, 1750 (2022)

53. R.B. Heimann, in *Trends in Biomaterials Research*. ed. by P. Pannone (Nova Science Publisher, 2007), pp.1–81

54. C. De Ruijter, J. Bos, H. Boerstoel, T.J. Dingemans, J. Polym. Sci. Part A Polym. Chem. **46**, 6565 (2008)

55. National Center of Biotechnology, https://www.ncbi.nlm.nih.gov/Books/NBK524853/ 524853 (2023)

56. V. Fournier, A. Quet, E. Meillot, H. Ageorges, Surf. Coat. Technol. **406**, 126744 (2021)

57. M.E. Orazem, N. Pébère, B. Tribollet, J. Electrochem. Soc.Electrochem. Soc. **153**, B129 (2006)

58. R.M. Souto, M.M. Laz, R.L. Reis, Biomaterials **24**, 4213 (2003)

59. T.M. Sridhar, U. Kamachi Mudali, M. Subbaiyan, Corros. Sci.. Sci. **45**, 237 (2003)

60. N.E. Putra, M.A. Leeflang, M. Minneboo, P. Taheri, L.E. Fratila-Apachitei, J.M.C. Mol, J. Zhou, A.A. Zadpoor, Acta Biomater. Biomater. **121**, 741 (2021)